PNAS RESEARCH ARTICLE | APPLIED PHYSICAL SCIENCES

Surface coating by mechanofusion modulates bulk charging pathways and battery performance of Ni-rich layered cathodes

Dong Hou[a,1], Jiaxiu Han[b,1], Chenxi Geng[c], Zhengrui Xu[a], Modhi M. AlMarzooqi[d], Jin Zhang[e], Zhijie Yang[a], Jungki Min[a], Xianghui Xiao[f], Olaf Borkiewicz[g], Kamila Wiaderek[g], Yijin Liu[e], Kejie Zhao[b,2], and Feng Lin[a,2]

Edited by Alexis Bell, University of California, Berkeley, CA; received July 26, 2022; accepted October 11, 2022

Ni-rich layered oxides as high-capacity battery cathodes suffer from degradation at high voltages. We utilize a dry surface modification method, mechanofusion (MF), to achieve enhanced battery stability. The simplicity, high yield, and flexibility make it cost-effective and highly attractive for processing at the industrial scale. The underlying mechanisms responsible for performance improvement are unveiled by a systematic study combining multiple probes, e.g., 3D nano-tomography, spectroscopic imaging, in situ synchrotron diffraction, and finite element analysis (FEA). MF affects the bulk crystallography by introducing partially disordered structure, microstrain, and local lattice variation. Furthermore, the crack initiation and propagation pattern during delithiation are regulated and the overall mechanical fracture is reduced after such surface coating. We validate that MF can alter the bulk charging pathways. Such a synergic effect between surface modification and bulk charge distribution is fundamentally important for designing next-generation battery cathode materials.

coating | charge heterogeneity | rechargeable batteries | tomography | in situ XRD

Significance

Surface coating is considered an effective way to mitigate performance degradation for polycrystalline cathodes in batteries. However, the synergic effect between surface modification, bulk charge distribution, and particle microstructural evolution has not been systematically studied. Moreover, many coating methods are practically expensive, require intermediate processing steps, and have high standards for precursors, etc. In this work, we use a facile method to prepare the coated polycrystalline cathode particles and then investigate the underlying mechanisms responsible for performance improvement using a combination of probes, e.g., nano-tomography, spectroscopic imaging, in situ diffraction, and finite element analysis. We believe that the revealed synergic effect by this study is a general feature that plays a vital role for the surface-coated polycrystalline cathodes in rechargeable batteries.

Alkali metal ion batteries (e.g., lithium-ion batteries) are considered the most effective energy storage candidate for portable electronics, power grids, and electric vehicles due to their considerable energy density, power density, cycle life, safety, and competitive prices (1). Achievements have been made progressively in pursuing batteries with higher energy and power density with the discovery of different types of high-capacity cathode materials. Over the past decade, polycrystalline ternary $LiNi_xMn_yCo_{1-x-y}O_2$ (NMC) layered oxides have been intensively investigated compared to other cathode material systems. The Ni-rich Co-less NMC (Ni ≥ 80%) is considered one of the most promising cathode materials due to its high discharge capacity (> 200 mAh g^{-1}) and high energy density (> 750 Wh kg^{-1}) (2). Reversible battery operation requires long-term stability, while common issues in these Ni-rich NMCs are the poor cycling performance and undesired degradation due to a combination of multiple factors (e.g., oxygen release, microcracking, phase transition). Different types of approaches have been explored, such as bulk doping (3), concentration gradient design (4), grain engineering (5–7), and surface/interface modifications (8). Among these methods, surface modification emphasizes building electrochemically robust interfacial layers, tuning local cation–anion chemical coordination environments, and eliminating undesired electrode–electrolyte side reactions. Such surface-level modulation is believed to preserve polycrystalline secondary particles and is responsible for mitigating performance degradation and enabling better electrochemical reversibility (9).

There are several commonly accepted explanations for the effect of surface coating on polycrystalline cathodes. Based on these proposed mechanisms, different types of coating layers were designed and implicated into cathodes. For example, Li et al. reported a solid electrolyte Li_3PO_4 coating on NMC by atomic layer deposition (ALD), which can work as a barrier to electrolyte infiltration (10). Some other coating layer works as HF scavengers, such as $MgAl_2O_4$ on $LiCoO_2$ (11), Al_2O_3 on NMC (12, 13), and $Co_3(PO_4)_2$ on $LiNi_{0.8}Co_{0.16}Al_{0.04}O_2$ (14). These chemically robust coating layers can consume the hazardous HF, mitigating the undesired reaction between the electrolyte and active cathode particles, such as transition metal (TM) dissolution and electrolyte decomposition (1). However, some aforementioned coating methods, such as ALD, can be expensive and have high requirements for precursors; some wet chemistry methods require a solution environment during coating, which produces waste liquid and requires filtering and additional drying/heating steps (15). All these drawbacks make surface coating less appealing for industrial-scale cathode processing.

Recently, a dry surface modification method, mechanofusion (MF), was reported for battery applications (15–17). The MF originated from the subject of dry coating or ordered mixing, which utilizes a combination of high shear and compression forces on the host and guest particles without liquid addition, creating chemical as well as physical surface

Author contributions: D.H., K.Z., and F.L. designed research; D.H., J.H., C.G., Z.X., M.M.A., J.Z., Z.Y., J.M., X.X., O.B., K.W., Y.L., K.Z., and F.L. performed research; D.H., J.H., K.Z., and F.L. analyzed data; and D.H., J.H., K.Z., and F.L. wrote the paper.

The authors declare no competing interest.

This article is a PNAS Direct Submission.

Copyright © 2022 the Author(s). Published by PNAS. This article is distributed under Creative Commons Attribution-NonCommercial-NoDerivatives License 4.0 (CC BY-NC-ND).

[1]D.H. and J.H. contributed equally to this work.

[2]To whom correspondence may be addressed. Email: kjzhao@purdue.edu or fenglin@vt.edu.

This article contains supporting information online at https://www.pnas.org/lookup/suppl/doi:10.1073/pnas.2212802119/-/DCSupplemental.

Published December 1, 2022.

Downloaded from https://www.pnas.org by PURDUE UNIVERSITY LIBRARY on December 1, 2022 from IP address 128.210.126.199.

interactions (fusion) between the particles (18). The simplicity, high yield, and flexibility of MF make it cost-effective and highly attractive for processing at the industrial scale. Note that other terminologies were used in this field, such as "dry particle fusion coating," "dry particle micro-granulation," or even oversimplified as "dry surface coating/doping," which are referring the same MF treatment (18). Unlike most techniques for performance improvement (e.g., doping, concentration gradient, grain engineering), in which modification happens before/during the NMC calcination, MF for surface coating can be a postsynthesis step, meaning that the process does not intertwine with the common synthesis factors (e.g., heating profile, atmospheres, precursor choices); therefore, the performance can be tuned independently and precisely after the NMC fabrication. Using MF for hetero-phasic surface coating has emerged in the community recently, such as coating carbon, Al_2O_3, SiO_2, and Nd_2O_5 on NMC (17, 19, 20).

Despite the achievements and wide applications of surface modifications on polycrystalline cathodes, an important question remains: what are the exact mechanisms/functions of surface coating on the stability improvements? Answering this question can guide the decision on various coating materials and coating techniques for battery manufacturing. Here, we hypothesize that the coating layer can modulate charging pathways inside secondary particles as well as the battery stability by offering physical confinement and redistributing ion transport. Validating this hypothesis entails probing the complex crystallographic, chemical, and morphological transformations in battery materials at various length scales, calling for a combination of different probes and data analytics strategies. In this study, we chose Ni-rich NMC (Ni content ~80%) as the platform for the MF process and then confirmed the stability improvements in cells using electrochemical diagnostics. We designed experiments using multiscale spectroscopic, scattering, and imaging probes, coupled with finite element analysis (FEA), to understand the fundamental correlation between surface coating, charge heterogeneity, phase transition, mechanical fracture, and battery stability.

Results

MF for Surface Coating on NMCs. Here, we adopted the MF process without foreign guest materials; the small NMC particles after batch solid-state synthesis serve as the guest while the large ones as the host and are referred to as "self-consumption coating," similar to the study by Zheng et al. (15). Fig. 1*A* illustrates the schematic and principle of the MF process. During high-speed rotation of the chamber, the centrifugal force and force from the press head squeeze powders on the chamber wall, while the scraper detaches the particles from the wall right after. The high compression and shear forces are applied to the particles during each rotation cycle. Repeating this process for an extended period leads to a coating layer on the particles. A detailed description of the working principle and design modification specified for electrode particles at the laboratory scale can be found in the study by Geng et al. (16). Fig. 1*B* is the scanning electron microscopy (SEM) of a pristine NMC particle after calcination, showing the individual grains with a size of hundreds of nanometers agglomerate into the large secondary particles. Obvious voids/pinholes and rough surfaces are common features for polycrystalline secondary particles. Fig. 1 *C* and *D* show the intact particles after MF coating. The surface is significantly smoothed, and a cross-section view in Fig. 1*D* shows a uniform coating layer with a thickness of 160 ± 20 nm. Analysis of multiple SEM images in *SI Appendix*, Fig. S1 proves a more uniform size for secondary particles after MF coating, and the fragments/debris are significantly decreased due to the collision and fusion with larger particles, validating the "self-consumption" process. Note that as shown in *SI Appendix*, Fig. S1 *D* and *E*, some particles remain uncoated, suggesting that not all the particles in the same batch were processed/smoothed at the same level. This is caused by the incomplete contact/interaction of powders at the very top and bottom of the rotation chamber. Such issue can be alleviated by pausing the fusion process and giving extra intermediate mixing from time to time, or simply by increasing the processing time.

Synchrotron X-ray diffraction (SXRD) in *SI Appendix*, Fig. S2 shows that the as-calcined NMC has a phase pure $R\bar{3}m$ layered structure, while the MF process does not induce impurity or discernible phase transition. Zoom-in of the SXRD patterns and directly comparing the peaks (*Panel a* vs. *b* in *SI Appendix*, Fig. S3) revealed that subtle yet important microstructure changes were introduced by the MF process. The peak becomes wider and less symmetric, with longer tails, indicating a deviation from well-ordered $R\bar{3}m$ atomic arrangement. The deviation can be justified by peak fitting of selected reflections. For example, incorporating a "diffuse" peak can enhance the fitting of the asymmetric 104 reflection of the MF-coated pattern (*Panel c* vs. *e* in *SI Appendix*, Fig. S3), while the clear long tails for 108/110 reflections can be compensated by an additional broad peak (*Panel d* vs. *f* in *SI Appendix*, Fig. S3). These extra diffuse signals underneath the coherent elastic scattering indicate the presence of local scale lattice inhomogeneity, as a result of microstrain variation (nonuniform lattice strain) inside the particles or between different particles.

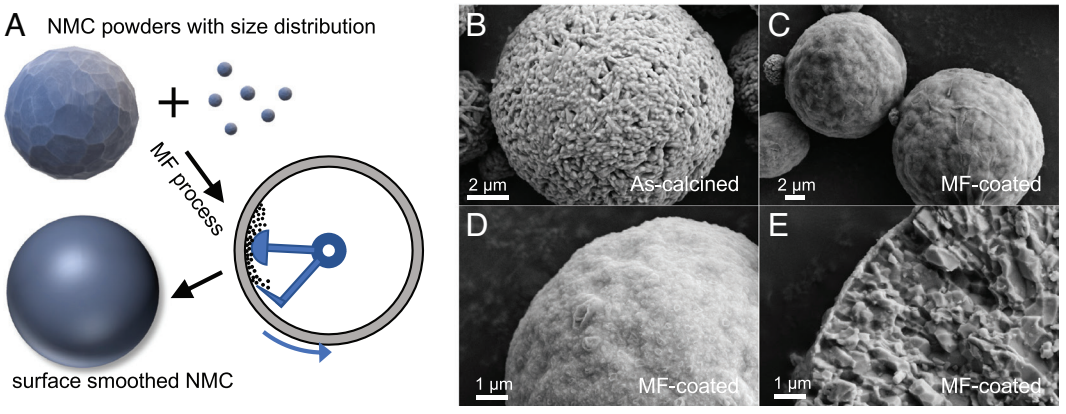

Fig. 1. MF on NMC powders without foreign additives. (*A*) Schematic setup of the MF process. (*B*) SEM of NMC secondary particles before the MF process. (*C*), (*D*) SEM of NMC secondary particles after the MF process. (*E*) Cross-section of an MF-coated NMC particle, showing a thin and uniform coating layer.

Downloaded from https://www.pnas.org by PURDUE UNIVERSITY LIBRARY on December 1, 2022 from IP address 128.210.126.199.

The observed SXRD difference was confirmed by Rietveld refinement, showing that the microstrain has a distinct increment after the MF process, from 0.0914 ± 0.0125% to 0.2114 ± 0.0255%. Representative fits for both samples and tabulated structural details can be found in *SI Appendix*, Fig. S4 and Table S1, respectively. Besides the microstrain, MF leads to slightly increased lattice parameters (majorly the expansion of cell length *a*, giving a 0.167% unit cell volume change), resulting in macroscopic strain by lattice change in the material. Moreover, the selected area electron diffraction pattern of the coating layer shows evidence that the MF processed surface might be a highly disordered phase, in which the amorphous feature is prominent (21). To summarize, our SXRD patterns, peak fitting, and full-profile refinements suggest that MF destructs the crystal structures on the surface and introduces partially disordered structure, microstrain, and local lattice variation in the bulk.

Crystal Structural and Morphological Changes during Delithiation. To better understand the correlation between the surface coating and final performance, it is crucial to study the chemistry, morphology, and crystallographic features in delithiated NMCs. Chemically delithiated NMC samples were prepared for the as-calcined and MF-coated batches. The degree of delithiation ranges from 35% to 65% and is referred to mild, medium, and deep delithiation batches as follows. The exact percentage of delithiation for each sample was validated by inductively coupled plasma-mass spectrometry (ICP-MS), and the cation ratios are reported in *SI Appendix*, Table S2.

SI Appendix, Fig. S5 shows the SXRD pattern changes as a function of delithiation level for MF-coated NMCs. A single H2 phase was observed in mild delithiated NMC, while further delithiation results in peak shift and broadening, suggesting gradual phase changes, consistent with observations on chemically delithiated NMCs in literature (22). For SXRD with higher Li removal, a considerable peak broadening, plus strong shifts, indicates the collapse of the layered structure under severe delithiation. The observation of a shoulder near the 003 reflection in 55% delithiated samples indicates the formation of an H3 phase, which was also reported in electrodes charged to high voltage (23, 24). Nonetheless, the bulk structural behavior of the chemically delithiated NMCs in this study is similar to the in situ cycling behaviors of NMC cells in literature, analogous to the electrochemical process. *SI Appendix*, Fig. S6 compares SXRD of as-calcined and MF-coated NMCs after 65% delithiation. The MF-coated one has less lattice change and sharper reflections, especially in high-*Q* region, indicating better crystallinity and a more robust crystal structure after MF coating.

Full-field transmission X-ray microscopy (TXM) was used to investigate the effect of surface coating on the stability of delithiated samples at the secondary particle level. The X-rays used in our TXM measurements have energies around Ni K-edge (~8350 eV) and thus can penetrate through particles, enabling nondestructive 3D visualization of the internal morphology of NMCs. Fig. 2 *A* and *E* depicts the 3D renderings of as-calcined and MF-coated NMC particles before delithiation, respectively. Similar to the observation from SEM, as-calcined NMC shows a rough surface, while MF-coated one is smoothed. Note that the identified voids/cracks near the surface in pristine MF-coated NMC are the gap between the coating layer and subsurface grains, not the intrinsic defects on the surface.

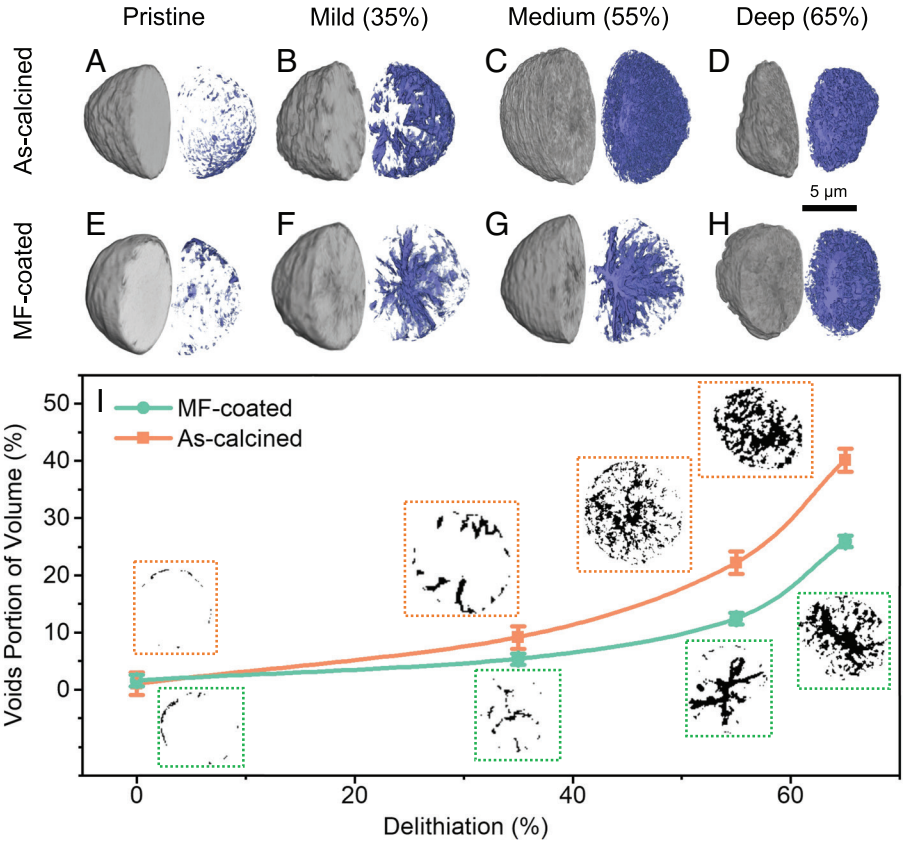

Fig. 2. Evolution of the particle morphology upon delithiation. (*A–D*) for as-calcined NMCs, while (*E–H*) for MF-coated ones. For each particle in *A–H*, the left hemisphere is 3D rendering (in gray scale) of the secondary particle structure, while the right hemisphere is the void volume (in blue) within the particle. (*I*) Quantification of the void fraction as a function of delithiation, with representative 2D slices of each particle as *Inset*.

Downloaded from https://www.pnas.org by PURDUE UNIVERSITY LIBRARY on December 1, 2022 from IP address 128.210.126.199.

The surface and internal changes as a function of delithiation levels are shown in Fig. 2 *A–D* and *E–H* for both NMCs. Note that microcracks inside the particles can be unveiled and quantified, while single grains or the grain boundaries cannot be resolved under the current TXM spatial resolution. We classified the microcracks into two categories (shown in *SI Appendix*, Fig. S7) using two representative particles: the first type for cracks initiated on the surface due to the attack from the electrolyte in cells or from oxidant during chemical delithiation, as shown in *SI Appendix*, Fig. S7 *A–C*, and the other is for radially aligned large cracks which coalesce near the particle center, as shown in *SI Appendix*, Fig. S7 *D–F*. During Li removal, anisotropic grain changes in secondary particles can lead to the accumulation of internal mechanical stress, and when the local stress reaches the particle's mechanical strength, these radial cracks are generated to release the strain energy. For the as-calcined NMC without a coating layer, the intergranular microcracks are mainly initiated on the surface and propagate inside under mild delithiation conditions. With further delithiation, a hollow interior and large crack forms due to the accumulation of voids, the detachment of single grains, and movements of grain boundaries. Such internal morphology is also commonly observed by cross-section SEM or TXM in highly delithiated cathodes (25, 26). Under deep delithiation, the microcracks pervade the entire secondary particle, as shown in Fig. 2*D*. For MF-coated NMC, the most distinct behavior was observed under mild and medium delithiation (Fig. 2 *F* and *G*), where the crack amount is less, and no serious aggregation of microcracks on the surface either. Instead, the most noticeable cracks are radially aligned. Note that the coating layer offers good protection to a certain degree, but deep delithiation will ultimately destroy the coating layer, as shown in Fig. 2*H*. The relative ratio between the internal crack and the particle volume is shown in Fig. 2*I*, where the MF-coated particle has fewer microcracks and voids under high delithiation.

In summary, cracks on the surface can accelerate the solution penetration into the particles (oxidant liquid for chemical delithiation and electrolyte for electrochemical delithiation). Such liquid penetration results in a harsh side reaction on cathodes, accompanied by other phenomena such as TM dissolution, surface reconstruction, and oxygen release. And, these events will in turn accelerate the crack formation process and the capacity deteriorates upon long-term cycling. Surface coating by MF can alter the crack initiation and propagation pattern and reduce the overall microcracks/void presence during delithiation.

MF Alters the Surface and Bulk Chemistry in NMCs. The 3D nano-tomography can be combined with X-ray Absorption Near-Edge Structure spectroscopic imaging (XANES-3DTXM), offering information on TM oxidation states within particles. In this work, Ni was chosen considering it as the major redox-active element in Ni-rich cathodes. The fitted white-line energy from Ni XANES spectra was used as an indicator of the local state of charge (SoC) in the particles. More details of the XANES-3DTXM data processing principles can be found elsewhere (27, 28). Fig. 3 *A* and *B* show the color-coded Ni white-line energies for pristine as-calcined and MF-coated NMCs, respectively. Higher energy represents a higher Ni oxidation state; in other words, a higher local SoC in cathode particles. Note that even before any delithiation, inhomogeneous Ni oxidation state distribution is observed, which might attribute to the intrinsic reaction heterogeneity during synthesis (29). Fig. 3 *C* and *D* show the SoC distribution for these NMCs after a mild delithiation, while 3D maps at other delithiation levels can be found in *SI Appendix*, Fig. S8. For both NMCs, delithiation results in local SoC heterogeneity, justified by the broader histogram distributions with increasing delithiation in *SI Appendix*, Fig. S8 *I* and *J*. Delithiation leads to the increase of Ni white-line energy, due to the gradual oxidation of Ni. The general SoC behavior trend agrees with that of previous studies on similar material systems (5, 24), justifying the XANES-3DTXM approach we used here.

Panel E vs. *F* in Fig. 3 shows a direct comparison of the SoC histograms between as-calcined and MF-coated NMCs. After delithiation, MF-coated NMC has slightly lower white-line energy, a less symmetric shape, and a longer low-energy "tail" of the distribution profile. To better illustrate the effect of MF on SoC distribution, we highlight the extremely low/high SoC nanodomains inside secondary particles in Fig. 3 *E* and *F* along with their distribution profiles. These local areas reaching upper/lower SoC limit might not account for a considerable portion of the total mass/volume of the battery, being neglected/averaged out during routine analysis. However, undesired chemomechanical events (e.g., overcharging, domain deactivation, oxygen release) are likely to happen easily in these regions, significantly impacting the capacity, impedance, and stability (30). The high/low SoC nanodomains were identified by voxels whose energies are beyond $[\mu - 2\sigma, \mu + 2\sigma]$, where μ is the mean white-line energy and σ is the SD for each particle's histogram. Therefore, the *Insets* in Fig. 3 *E* and *F* only present the top or bottom 2.2% of the total voxels with extremely high or low SoC values.

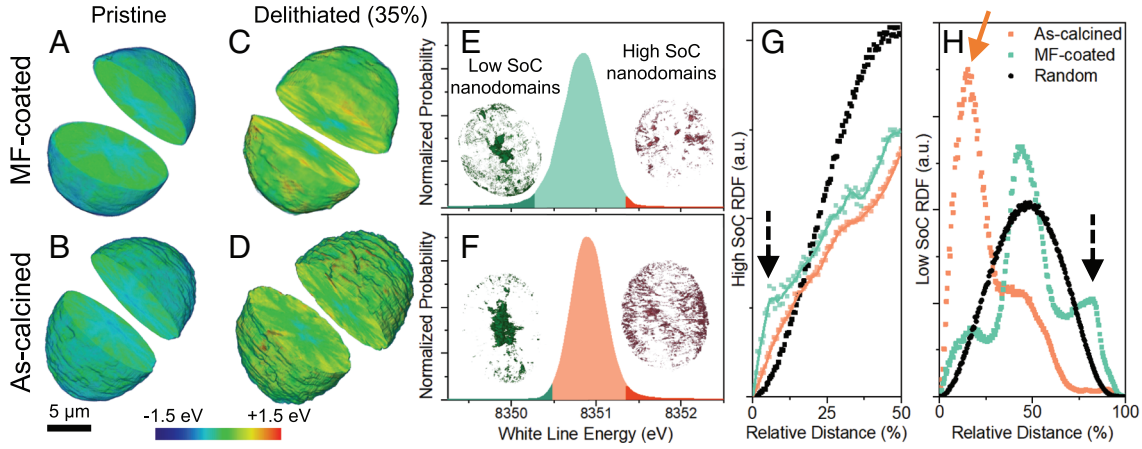

Fig. 3. SoC distribution in NMC particles. 3D rendering of Ni white-line energy for (*A*) as-calcined and (*B*) MF-coated NMCs in the pristine form. The same set plots after delithiation are shown in (*C* and *D*). Mild delithiation (35%) was used for demonstration here. The Ni white-line energies are color coded, where blue and red stand for low and high oxidation states, respectively. The SoC histogram of white-line energies for delithiated (*E*) as-calcined NMCs and (*F*) MF-coated ones. *Insets* visualize the high/low SoC nanodomain distribution. RDFs of (*G*) high SoC and (*H*) low SoC nanodomains after delithiation.

Downloaded from https://www.pnas.org by PURDUE UNIVERSITY LIBRARY on December 1, 2022 from IP address 128.210.126.199.

For the high SoC nanodomains (red 3D renderings in Fig. 3 *E* and *F*) inside delithiated NMCs, the as-calcined ones show dispersed distribution over the whole particle, while nanodomains are more aggregated in MF-coated ones with larger SoC clusters. Therefore, there are fewer active locations in the bulk of MF-coated NMC for intrinsic chemomechanical events, mitigating internal stress buildup and degradation. Inspired by radial distribution functions (RDFs) in crystallography, we adopted a method to analyze the relative distance between each voxel and quantify the SoC nanodomains. Fig. 3*G* plots the RDFs of high SoC nanodomains (hot spots) for as-calcined and MF-coated NMCs after delithiation, together with the simulated RDF from a particle with randomly distributed nanodomains inside, which follows the ideal Gaussian shape. An obvious jump of the RDF shoulder at the very short distance region is observed for MF-coated NMC (dashed arrow in Fig. 3*G*), indicating the existence of larger local clusters, which agrees with the visual observation. Moreover, quantitative analysis shows that high SoC nanodomains occupy 27.9% volume of the surface shell (assuming a thickness of 0.16 μm) for as-calcined NMC after delithiation, while only 13.8% of the surface shell consists of high SoC domains in MF-coated counterparts, further proving that coating can reduce the "hot spots" on the surface by introducing a Ni-deactivated layer.

For the low SoC nanodomains inside delithiated NMCs (green 3D renderings in Fig. 3 *E* and *F*), MF-coated ones resemble a shell, attributing to the amorphous-like disordered outer layer. Note that the low SoC shell preserves after mild to medium delithiation for MF-coated NMCs, while extreme delithiation will destroy the shell eventually. While for the as-calcined ones, the low SoC nanodomains enrich inward after delithiation. Such distribution inherits from the pristine particles, where incomplete oxidation of Ni happens during calcination. This is also represented by the RDF peak at the short distance region (orange arrow) in Fig. 3*H*. Such a nonequilibrium state is widely reported in the literature (26, 29, 31). In the coating layer, Ni is deactivated and serves as protection for NMCs from cathode–electrolyte side reactions, thus contributing to the chemical stability under delithiation. Distinct RDF features for MF-coated NMCs, e.g., the emergence of a peak at a long distance (dashed arrow) and decreased peak height at a short distance (orange arrow), indicate the formation of a low SoC shell and the disappearance of a less active core.

In summary, the XANES-TXM study on chemically delithiated NMCs proves that MF coating can alter the Ni oxidation state and the charge behaviors of NMCs on the surface as well as inside the secondary particle. The active regions are more aggregated in the bulk after MF coating, mitigating the local chemomechanical events during delithiation. The Ni-deactivated passivation layer introduced by MF can protect the surface from cathode–electrolyte side reactions, improving stability.

MF Modulates Charge Behavior, Lattice Change, and Battery Performance. Electrochemical measurements were performed to further validate the improved stability of MF coating. Fig. 4 *A* and *B* (together with *SI Appendix*, Figs. S9 and S10) shows that MF-coated cells have a comparable initial discharge capacity with the as-calcined ones under 1 C rate, while retention after 50 cycles is enhanced from 85.9 ± 1.2% to 93.0 ± 1.3%. Our electrochemical tests agree well with those of other reported studies on the MF-coated cathodes (21, 32). The cells were dissembled after 50 cycles at the 4.5 V charged state, and then powders were collected from the cathode disk for ex situ XANES-3DTXM measurements.

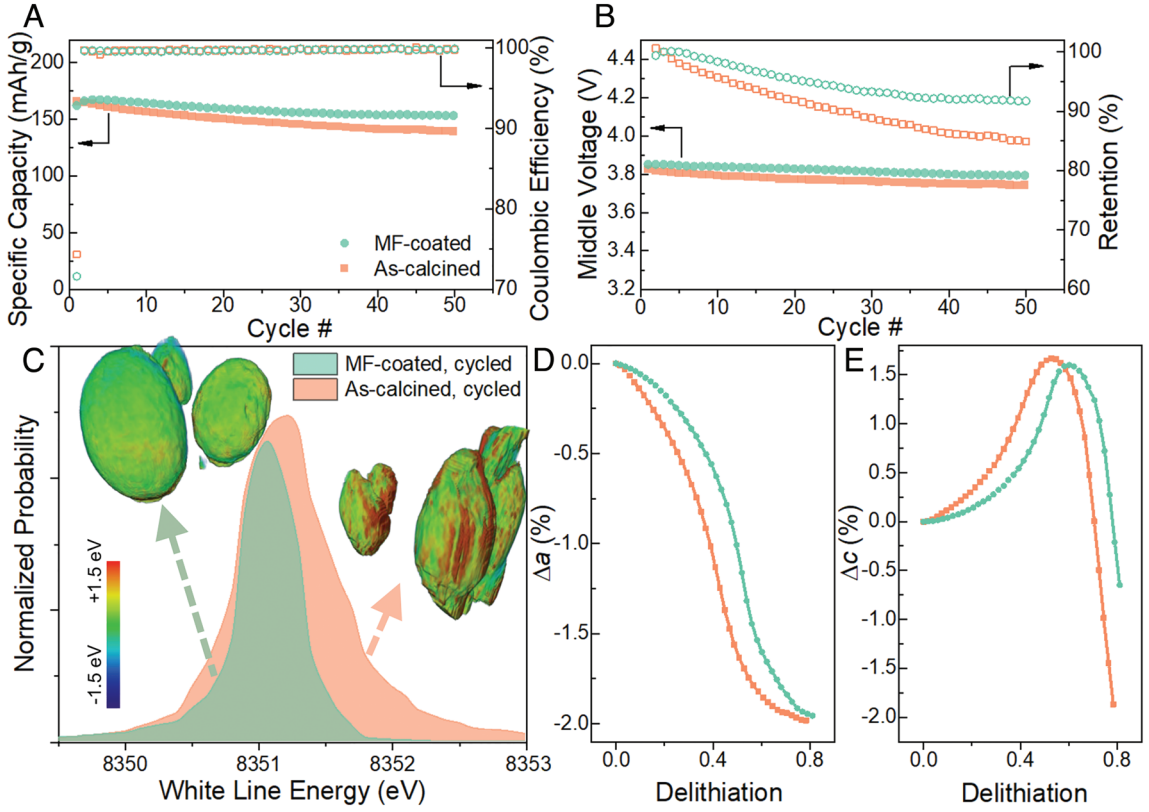

Fig. 4. Battery performance, charge behavior, and lattice change. (*A* and *B*) Specific capacity, coulombic efficiency, middle voltage, and retention of the as-calcined and MF-coated NMCs at 1 C and 25°C. (*C*) 3D rendering and histogram of SoC distribution in NMC particles after 50 cycles. (*D* and *E*) Relative changes of lattice parameters during charging from in situ cycling SXRD. Note that *D* and *E* are the statistically averaged results of many particles inside the in situ cells.

Downloaded from https://www.pnas.org by PURDUE UNIVERSITY LIBRARY on December 1, 2022 from IP address 128.210.126.199.

Fig. 4*C* shows the 3D rendering of local SoC distribution for a few representative NMC particles from these cycled cells. The histogram is sharper for MF-coated NMCs, meaning that the local SoC is more uniform and homogenous, while the as-calcined particles are more heterogeneous. Such difference is further supported by the more oxidized surface for as-calcined NMCs after 50 cycles, while the surface of the MF-coated ones remains at a low oxidation state.

In situ SXRD during the first charge was performed and the collected patterns can be found in *SI Appendix*, Fig. S11 for both NMC cells. In situ SXRD serves as a bulk probe, presenting the statistically averaged behavior of many particles. The lattice parameters were extracted by Le Bail fit (33), and the changes of lattice parameters (length *a* and *c*) relative to their pristine states were plotted in Fig. 4 *D* and *E*. The as-calcined NMCs incline to lattice change under delithiation, especially at the early stage of charging, and after deep delithiation, a large *c* decrement of 2.0% is obtained, on the same level of the observation from other groups on similar compositions (34, 35), while the MF-coated ones are reluctant to lattice distortion and phase transition, being more robust to Li removal. This is evidenced by the *c* decrement of only 0.6% (vs. 2.0% from as-calcined NMC) at the highly delithiated stage. The anisotropic lattice change during charging will lead to the accumulation of internal mechanical stress and local strain field, which will eventually be released through grain disintegration and crack formation/prorogation.

We performed theoretical modeling to understand the modulation of MF coating on charge heterogeneity, lattice change, and intergranular damage in the NMC polycrystalline particles. To achieve a qualitative understanding, we constructed a simplified model composed of one-quarter of an NMC polycrystalline particle and simulated the coevolution of the Li/charge distribution, stress/strain, and intergranular fracture upon charging using FEA. The detailed procedure of model construction is described in the *Methods* section and our previous work (36, 37). Briefly, Li concentration distribution is solved by the kinetics of diffusion. The mechanics field is solved by the standard equations of deformation kinematics, constitutive relationship, and mechanical equilibrium. The evolution of intergranular fractures is determined by the interfacial damage function along the grain boundary.

We hypothesize that the MF coating improves the mechanical stability of NMC due to two mechanisms. First, the disordered MF coating layer promotes the charge transfer reaction at the surface of the NMC particle by providing a fast path to distribute Li over the entire particle surface (38). Such enhanced Li transport minimizes the heterogeneity of the charge distribution and reduces the locally accumulated mechanical stress and damage. A schematic is illustrated in Fig. 5*A*. To implement this mechanism, we set an isotropic Li diffusivity in the disordered MF layer which is equal to the Li diffusivity along the *ab*-plane in the NMC lattice. Second, the coating-protected NMC particles experience reduced lattice changes upon charging, which mitigates the mismatch strain at grain boundaries and thus the intergranular fracture. To simulate the variation of Li access at different locations on the NMC particle surface, we prescribe various Li flux boundary conditions shown in Fig. 5*B*. Such a variation in the real batteries is caused by the incomplete contact of the NMC particle to the electron-conducting network or the coverage of the insulating polymer binder. The prescribed boundary condition naturally induces a global charge heterogeneity in NMC. We build an MF layer that is uniformly coated on the NMC particle (Fig. 5*A*). Through the in situ SXRD experiments, we observe that the MF-coated NMC experiences fewer changes in the lattice parameters than that of the bare NMC particles (*Panel D* vs. *E* in Fig. 4). Therefore, in the FEA modeling, we apply the experimentally measured anisotropic deformation along the *a*- and *c*-axials as a

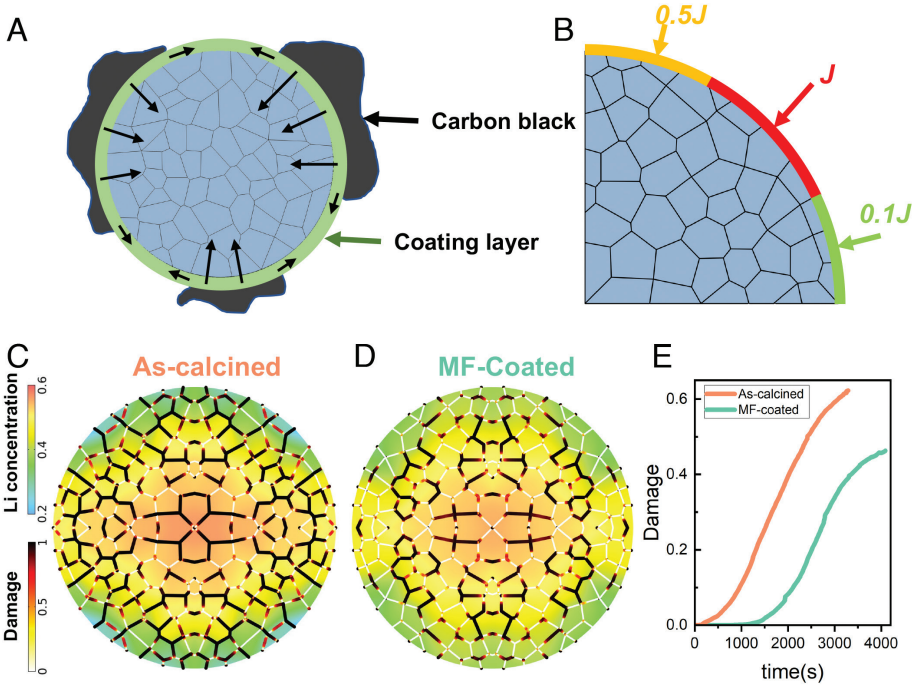

Fig. 5. FEA results. (*A*) Schematic of an MF-coated NMC secondary particle showing that the disordered coating layer promotes Li transport over the particle surface and intercalation into the NMC grains. (*B*) An NMC polycrystalline model with various Li flux boundary conditions to mimic the variation of Li access at different locations on the particle surface. (*C* and *D*) Li concentration distribution and intergranular damage at the SoC of 55% in as-calcined and MF-coated NMCs, respectively. The dark-red scheme represents the intergranular damage, and the rainbow color represents the Li concentration. (*E*) Time evolution of the intergranular damage in as-calcined and MF-coated NMCs.

Downloaded from https://www.pnas.org by PURDUE UNIVERSITY LIBRARY on December 1, 2022 from IP address 128.210.126.199.

function of the SoC for the MF-coated and as-calcined NMCs. The anisotropic strains and random orientation of the primary particles lead to the accumulated mismatch strain at grain boundaries. Such mismatch strains are the major cause of the formation and propagation of intergranular cracks.

Fig. 5 *C* and *D* show the Li concentration and damage distribution at the delithiation state of ~55% for the as-calcined and MF-coated NMCs. For a better visual presentation, the results in the one-quarter model have been expanded to the entire circular domain by a mirror operation. Overall, the coated NMC shows much less global charge heterogeneity and intergranular damage. The disordered coating layer serves as an isotropic Li transport channel, which effectively promotes Li distribution compared to that in the anisotropic lattice. The isotropic Li highway minimizes the impact of the different Li accesses between the local regions of the NMC particle surface, which reduces the charge heterogeneity and mechanical stresses. It is noteworthy that rare cracks are observed at the surface of the MF-coated particle. Li extraction from NMC induces an overall tensile stress in the bulk of the particle. To balance this tension inside particles, the coating layer experiences an overall compressive stress, which reduces the driving force of crack opening along the grain boundaries. The charge homogeneity and mechanical confinement of the coating layer contribute jointly to the crack mitigation at the surface. The evolution of the Li concentration distribution and intergranular damage during the charging process for two NMC models are shown in Movie S1 (as-calcined) and Movie S2 (MF-coated). Fig. 5*E* summarizes the key result, where the much-reduced mechanical damage in the MF-coated NMC demonstrates that the coating layer improves the mechanical robustness of NMC polycrystalline particles against the cyclic structural degradation. Our theoretical modeling agrees well with the experimental observation and provides a mechanistic understanding of the important role of MF coating on NMC.

Discussion

In summary, a facile surface modification method, MF, was applied to the Ni-rich NMCs as a postsynthesis step ready for industrial-scale production. The enhanced cycling stability without compromise of capacity was confirmed in the MF-coated NMC cells. Ex situ SXRD of chemically delithiated powders and in situ SXRD of electrochemically delithiated cells reveal superior crystallographic integrity and robustness, while XANES-3DTXM proves a modulated charging pathway and crack propagation pattern during delithiation after the MF coating process. Together with FEA simulation and other experimental probes (e.g., SEM, ICP-MS), we discovered the synergic effect between surface modification, bulk charge heterogeneity, mechanical fracture, and local stress/strain:

1. The physical confinement from MF surface coating alters the charge distribution inside secondary particles, resulting in a Ni-deactivated passivation layer and fewer high SoC hot spots for intrinsic chemomechanical events in the bulk.
2. The smoothed disordered layer provides isotropic Li transport paths, which spreads Li-ions uniformly and effectively, leading to an improved effective Li diffusivity. Meanwhile, better contact with carbon black due to the smooth surface facilitates the electrical conductivity during charging.

Both mechanisms contribute to the modulated charge behavior inside the MF-coated particles, and furthermore, lead to the robust crystal structure during charging, being more invulnerable to internal mechanical stress/strain. Subsequently, the most obvious outcome is the enhanced mechanical durability, less mechanical disintegration, and fewer fractures/cracks for NMC secondary particles, ultimately leading to more stable battery performance.

A recent work by Li et al. (39) built an interpretable machine learning framework to identify the most important attributes of polycrystalline NMCs to the cell performance. Based on such statistical analysis, it was claimed that in the early cycles the individual particles' features (such as individual particle morphology, chemistry, and position) dominate the degree of damage. Here, our study provides another experimental evidence for the statement by Li et al. The MF process smooths the surface and homogenizes the charge distribution inside the particle, which are directly correlated to the morphological attributes and chemical characteristics identified by the machine learning framework, contributing to the mitigated reaction and damage heterogeneity in the early cycles. Moreover, Li et al. claimed that in the later cycles the interaction between neighboring particles (such as packing density, contact area, and neighboring particle morphology) plays an important role for the degradation. Since MF only modulates the particles' self-attribute while the interaction between neighboring particles maintains largely unaffected, we speculate that the damages arise from such aspects and the synchronous group behavior might be similar between the MF-coated and as-calcined samples.

Although this work focuses on the MF of the cathode materials, it is still worth noting that such treatment can also be beneficial to anodes. The MF treatment on anode materials could enhance the lithium diffusivity by offering isotropic Li transport paths, similar to the observation on MF-coated NMCs. Moreover, it might form an extra passivation layer between the solid electrolyte interphase (SEI) and bulk anode, therefore modulating the SEI stability. MF process can also facilitate the discovery of new types of anode materials. For example, silicon–graphite composites were reported by Cao et al. (40) using the MF process, in which silicon alloy particles can be well dispersed and embedded between graphite layers. As a result of this unique arrangement, cyclability and rate capability are enhanced in the batteries.

Our study demonstrated that for cathode surface modification, multiple factors/mechanisms simultaneously contribute to the final battery performance. To better control the modification process, these factors need to be deconvoluted using a combination of experimental probes at multiple length scales, as well as the support from theoretical modeling. A final note is that developing precise control of coating layer thickness is necessary for applying MF to various cathode material systems in the future. There is a balance between the rotation speed and processing time for a given thickness of coating layer and uniformity of the coated particles. Higher rotation speed will decrease the processing time but might undermine the integrity of the secondary particles due to larger shear and compression forces. On the contrary, lower speed can maintain the mild MF effect, but the processing time can be much longer. Studying how different combinations of MF processing parameters can lead to the thickness and uniformity variation and thereafter engineering the performance are a very interesting topic. Moreover, the layer thickness might vary for different cathode material systems given the same processing parameters. A detailed study of the correlation between the coating layer thickness, secondary particle behaviors, and performance is beneficial to researchers and engineers in the battery community.

Materials and Methods

Materials Synthesis. The NMC hydroxide precursor was obtained from a third party. The precursor was dried in a vacuum oven at 120°C for 12 h, then mixed

Downloaded from https://www.pnas.org by PURDUE UNIVERSITY LIBRARY on December 1, 2022 from IP address 128.210.126.199.

with LiOH (5% extra to compensate for the possible Li loss) thoroughly, and calcined under oxygen flow at 2.0 L min−1. The sample was heated from room temperature (RT) to 460°C with a rate of 5°C min−1, held for 2 h. Then, the sample was heated to 750°C at the same rate, following a holding period of 6 h. Later, the furnace was naturally cooled to RT under constant oxygen flow to obtain the as-calcined NMC powders. ~45 g of as-calcined NMC powders were loaded in a customized MF machine (16), with a spinning speed of 3,600 rpm for 60 min. The chemically delithiated NMC powders were prepared by mixing the pristine powder with the oxidant (0.1 mol L−1 NO2BF4 in acetonitrile medium) and stirred for 24 h inside the glovebox. The delithiated powder was then centrifuged and washed with pure acetonitrile four times to remove any NO2BF4 residual. The collected powder was then vacuum dried at 80°C for 12 h. The delithiation level is controlled by the amount of NO2BF4 in the oxidant solution.

Electrochemical Measurements. The composite cathode electrode was prepared using 90% active material, 5% polyvinylidene fluoride, and 5% acetylene carbon black in N-methyl-2-pyrrolidone and then cast onto carbon-coated aluminum foil current collectors. The electrodes were dried under vacuum at 120°C for 12 h without calendering. The dried electrode sheet was punched into disks with a diameter of 10 mm, an active material loading of 4.0 mg cm−2, and an approximately 70 μm thickness without including the current collector. The low-mass loading electrodes were chosen to minimize the impact of electrode polarization and to best reflect the intrinsic material properties. CR2032-type half cells were assembled in an Ar-filled glovebox (MBraun, O2 < 0.5 ppm, H2O < 0.5 ppm) using the electrode as the cathode, Li metal as the anode (450 μm in thickness and 15.6 mm in diameter), and Whatman glass fiber as the separator. The electrolyte was 1 mol L−1 LiPF6 dissolved in a 3:7 weight ratio of ethylene carbonate and ethyl methyl carbonate with 2 wt.% vinylene carbonate. The electrochemical testing of coin cells was performed on an electrochemical workstation (Wuhan Land Company). The performance data were measured under galvanostatic discharge/charge in the cutoff voltage range of 2.5–4.5 V at 22°C. 1 C was defined as fully charging the cathode in 1 h, with a specific capacity of 200 mAh g−1. After the cell was cycled and charged to the designated SoC, the cells were transferred to a glovebox immediately. The cathode disks were collected, rinsed with dimethyl carbonate, dried, and then sealed in Mylar aluminum bags in the glovebox for later use.

Material Characterization. The morphologies of NMC samples were investigated using LEO (Zeiss) 1550 field-emission SEM at an accelerating voltage of 5 kV. To determine the chemical composition of pristine and chemically delithiated NMC powders, the samples were dissolved in concentrated nitric acid, and then ICP-MS was performed on Thermo Electron X-Series ICP-MS analyzer.

The pristine and chemically delithiated NMC powders were loaded into TXM capillaries. The XANES-3DTXM was performed at beamline 6-2c at Stanford Synchrotron Radiation Lightsource (SSRL), SLAC National Accelerator Laboratory. An in-house developed software package known as TXM-Wizard was used to reconstruct and align the tomographic datasets at different X-ray exposure energies (41). The electrochemically delithiated powders were obtained from the cathode disk disassembled from cycled cells. XANES-3DTXM on such powders was performed at beamline 18-ID at National Synchrotron Light Source II (NSLS-II), Brookhaven National Laboratory. A scientific package, TXM-Sandbox, was used to reconstruct and align the tomographic datasets (42, 43). Ni K-edge white-line energy was extracted to benchmark the relative oxidation state of Ni by fitting the spectra in MATLAB with a combination of trigonometric and second-order polynomial functions for the best convergence. A commercial software, Amira-Avizo, was used for visualization. Extra information about the XANES-3DTXM can be found in *SI Appendix*, Note S1.

In situ SXRD was performed at beamline 11-ID-C at Advanced Photon Source (APS), Argonne National Laboratory, with a wavelength of 0.1173 Å (105.7 keV) using Argonne's multipurpose in situ X-ray (AMPIX) cell (44). The cathode pellet was prepared by mixing the NMC powders with carbon black and polytetrafluoroethylene uniformly. The pellet was mounted in the AMPIX cell with Li metal as anode. The electrolyte was the same as the one used in our CR2032 cells. SXRD images were obtained in the transmission geometry with a Perkin–Elmer flat-panel amorphous-silicon 2D detector. The datasets were continuously collected during charging the cell to 4.5 V with 0.1 C rate. CeO2 was used for calibration. Ex situ SXRD of powders was collected at beamline 28-ID-1 at NSLS-II with a wavelength of 0.1665 Å. The powder samples were loaded in Kapton capillaries, and patterns were recorded with a collection time of 20 s. Ni was used for calibration. The obtained 2D patterns were then integrated into 1D patterns using the DIOPTAS software (45). The Le Bail fit and Rietveld refinement were conducted using the software GSAS-II (46). Extra information can be found in *SI Appendix*, Note S2.

FEA. We simulate the Li concentration, stress, and intergranular fracture of an NMC polycrystalline particle during charging. We build a quarter of a circular domain composed of primary particles with random shapes and orientations. A quarter circular is efficient in modeling and sufficient to validate our hypothesis. The governing equation for Li diffusion is Fick's Law, $\frac{\partial c}{\partial t} = [D_{ij}c_{,j}]_{,i}$, where c is the Li concentration and D_{ij} is the anisotropic diffusivity. We assume that the diffusivity along the c direction is 1/10 of the diffusivity in the ab plane. The initial value of Li concentration is the maximum concentration in the pristine NMC. A constant flux boundary condition is prescribed on the surface. We set 1 C, 0.5 C, and 0.1 C on different grains of the particle to mimic the different access to Li on the particle surface. The deformation kinematics is described as $\varepsilon_{ij} = \frac{1}{2}(u_{i,j} + u_{j,i})$, where u is the displacement vector and ε_{ij} the total strain. The total strain is decomposed as $\varepsilon_{ij} = \varepsilon^{E}{}_{ij} + \varepsilon^{L}{}_{ij}$, where ε^{E} and ε^{L} represent the elastic strain and lithiation/delithiation induced strain, respectively. The delithiation-induced strain is calculated as $\varepsilon^{L} = \frac{l - l_0}{l_0}$, where l_0 and l are the lattice parameters of NMC at the pristine and current charged state, respectively. The lattice parameters in the two different NMCs are obtained from our in situ cycling SXRD experiments. The constitutive law $\sigma_{ij} = C_{ijkl}\varepsilon^{E}{}_{kl}$ describes the stress–strain relationship, where C_{ijkl} is the stiffness matrix. Mechanical equilibrium is prescribed as $\sigma_{ij,j} = 0$. We implement the cohesive zone method to simulate the crack generation and propagation. The damage function is calculated as $D = \begin{cases} 0, u < u_0 \\ \frac{u_f}{u_f - u_0} \times \left(1 - \frac{u_0}{u}\right), u_0 < u < u_f \\ 1, u > u_f \end{cases}$.

The damage parameter D remains zero when the separation is smaller than u_0, which is within the elastic response range. Damage equals one when the separation exceeds u_f, which is the fracture separation when the strain energy goes beyond the fracture energy. More details of the damage modeling can be found in our previous publications (36, 37). The governing equations of the kinetics of diffusion, deformation kinematics, and cohesive zone model are solved simultaneously using the commercial software COMSOL 5.6. Parameters used in FEA modeling are listed in *SI Appendix*, Table S3.

Data, Materials, and Software Availability. All study data are included in the article and/or *SI Appendix*.

ACKNOWLEDGMENTS. The work was supported by the NSF under Grant No. DMR-1832613. The work at Purdue was supported by NSF under Grant No. DMR-1832707. Use of the SSRL, SLAC National Accelerator Laboratory, is supported by the U.S. Department of Energy (DOE), Office of Science, Office of Basic Energy Sciences, under Contract No. DE-AC02-76SF00515. This research used resources of the NSLS-II, a U.S. DOE Office of Science User Facility operated for the DOE Office of Science by Brookhaven National Laboratory under Contract No. DE-SC0012704. This research used resources of the APS, a U.S. DOE Office of Science User Facility, operated for the DOE Office of Science by Argonne National Laboratory, under Contract No. DE-AC02-06CH11357. This work used shared facilities at the Virginia Tech National Center for Earth and Environmental Nanotechnology Infrastructure, a member of the National Nanotechnology Coordinated Infrastructure, supported by NSF (ECCS 1542100 and ECCS 2025151). We thank Dr. Lei Tao and Dr. Harry Charalambous for the help on in situ XRD measurements. The engineering supports from Kevin Beyer at APS beamline 11-ID-C and Gihan Kwon at NSLS-II beamline 28-ID-1 are gratefully acknowledged.

Author affiliations: [a]Department of Chemistry, Virginia Tech, Blacksburg, VA 24061; [b]School of Mechanical Engineering, Purdue University, West Lafayette, IN 47907; [c]Department of Physics and Atmosphere Science, Dalhousie University, Halifax, NS B3H 4R2, Canada; [d]Chemical and Biomolecular Engineering Department, University of California, Los Angeles, CA 90095; [e]Stanford Synchrotron Radiation Lightsource, Stanford Linear Accelerator Center (SLAC) National Accelerator Laboratory, Menlo Park, CA 94025; [f]National Synchrotron Light Source II, Brookhaven National Laboratory, Upton, NY 11973; and [g]Advanced Photon Source, Argonne National Laboratory, Lemont, IL 60439

Downloaded from https://www.pnas.org by PURDUE UNIVERSITY LIBRARY on December 1, 2022 from IP address 128.210.126.199.

1. Z. Xu, M. M. Rahman, L. Mu, Y. Liu, F. Lin, Chemomechanical behaviors of layered cathode materials in alkali metal ion batteries. *J. Mater. Chem. A* **6**, 21859–21884 (2018).
2. J. U. Choi, N. Voronina, Y. Sun, S. Myung, Recent progress and perspective of advanced high-energy Co-less Ni-rich cathodes for Li-ion batteries: Yesterday, today, and tomorrow. *Adv. Energy Mater.* **10**, 2002027 (2020).
3. L. Mu *et al.*, Structural and electrochemical impacts of Mg/Mn dual dopants on the $LiNiO_2$ cathode in Li-metal batteries. *ACS Appl. Mater. Interfaces* **12**, 12874–12882 (2020).
4. Y.-K. Sun *et al.*, High-energy cathode material for long-life and safe lithium batteries. *Nat. Mater.* **8**, 320–324 (2009).
5. Z. Xu *et al.*, Charge distribution guided by grain crystallographic orientations in polycrystalline battery materials. *Nat. Commun.* **11**, 83 (2020).
6. N. Park, H. Ryu, G. Park, T. Noh, Y. Sun, Optimized Ni-rich NCMA cathode for electric vehicle batteries. *Adv. Energy Mater.* **11**, 2003767 (2021).
7. D. Hou *et al.*, Effect of the grain arrangements on the thermal stability of polycrystalline nickel-rich lithium-based battery cathodes. *Nat. Commun.* **13**, 3437 (2022).
8. L. Yang *et al.*, Harnessing the surface structure to enable high-performance cathode materials for lithium-ion batteries. *Chem. Soc. Rev.* **49**, 4667–4680 (2020).
9. U. Nisar, N. Muralidharan, R. Essehli, R. Amin, I. Belharouak, Valuation of surface coatings in high-energy density lithium-ion battery cathode materials. *Energy Storage Mater.* **38**, 309–328 (2021).
10. X. Li *et al.*, Atomic layer deposition of solid-state electrolyte coated cathode materials with superior high-voltage cycling behavior for lithium ion battery application. *Energy Environ. Sci.* **7**, 768–778 (2014).
11. G.T.-K. Fey, Z.-F. Wang, C.-Z. Lu, T. P. Kumar, $MgAl_2O_4$ spinel-coated $LiCoO_2$ as long-cycling cathode materials. *J. Power Sources* **146**, 245–249 (2005).
12. A. M. Wise *et al.*, Effect of Al_2O_3 coating on stabilizing $LiNi_{0.4}Mn_{0.4}Co_{0.2}O_2$ cathodes. *Chem. Mater.* **27**, 6146–6154 (2015).
13. F. Dogan, J. T. Vaughey, H. Iddir, B. Key, Direct observation of lattice aluminum environments in Li ion cathodes $LiNi_{1-y-z}Co_yAl_2O_2$ and Al-doped $LiNi_xMn_yCo_z$. *ACS Appl. Mater. Interfaces* **8**, 16708–16717 (2016).
14. K. S. Ryu *et al.*, Effects of $Co_3(PO_4)_2$ coatings on $LiNi_{0.8}Co_{0.16}Al_{0.04}O_2$ cathodes during application of high current. *J. Appl. Electrochem.* **38**, 1385–1390 (2008).
15. L. Zheng, C. Wei, M. D. L. Garayt, J. MacInnis, M. N. Obrovac, Spherically smooth cathode particles by mechanofusion processing. *J. Electrochem. Soc.* **166**, A2924–A2927 (2019).
16. C. Geng *et al.*, A low-cost instrument for dry particle fusion coating of advanced electrode material particles at the laboratory scale. *J. Electrochem. Soc.* **167**, 110509 (2020).
17. M. N. Obrovac, L. Zheng, M. D. L. Garayt, Engineered particle synthesis by dry particle microgranulation. *Cell Rep. Phys. Sci.* **1**, 100063 (2020).
18. R. Pfeffer, R. N. Dave, D. Wei, M. Ramlakhan, Synthesis of engineered particulates with tailored properties using dry particle coating. *Powder Technol.* **117**, 40–67 (2001).
19. M. J. Herzog, N. Gauquelin, D. Esken, J. Verbeeck, J. Janek, Facile dry coating method of high-nickel cathode material by nanostructured fumed alumina (Al_2O_3) improving the performance of lithium-ion batteries. *Energy Technol.* **9**, 2100028 (2021).
20. Y. Shi *et al.*, Facile and scalable dry surface doping technique to enhance the electrochemical performance of $LiNi_{0.64}Mn_{0.2}Co_{0.16}O_2$ cathode materials. *J. Mater. Chem. A* **8**, 19866–19872 (2020).
21. L. Zheng, T. D. Hatchard, M. N. Obrovac, A high-quality mechanofusion coating for enhancing lithium-ion battery cathode material performance. *MRS Commun.* **9**, 245–250 (2019).
22. J. Alvarado *et al.*, Thermal stress-induced charge and structure heterogeneity in emerging cathode materials. *Mater. Today* **35**, 87–98 (2020).
23. W.-S. Yoon, K. Y. Chung, J. McBreen, X.-Q. Yang, A comparative study on structural changes of $LiCo_{1/3}Ni_{1/3}Mn_{1/3}O_2$ and $LiNi_{0.8}Co_{0.15}Al_{0.05}O_2$ during first charge using in situ XRD. *Electrochem. Commun.* **8**, 1257–1262 (2006).
24. C. Tian *et al.*, Distinct surface and bulk thermal behaviors of $LiNi_{0.8}Mn_{0.2}Co_{0.2}O_2$ cathode materials as a function of state of charge. *ACS Appl. Mater. Interfaces* **12**, 11643–11656 (2020).
25. H.-H. Ryu, K.-J. Park, C. S. Yoon, Sun, Capacity fading of Ni-rich $Li[Ni_xCo_yMn_{1-x-y}]O_2$ ($0.6 \le x \le 0.95$) cathodes for high-energy-density lithium-ion batteries: Bulk or surface degradation? *Chem. Mater.* **30**, 1155–1163 (2018).
26. Y. Mao *et al.*, High-voltage charging-induced strain, heterogeneity, and micro-cracks in secondary particles of a nickel-rich layered cathode material. *Adv. Funct. Mater.* **29**, 1900247 (2019).
27. Y. Liu, A. M. Kiss, D. H. Larsson, F. Yang, P. Pianetta, To get the most out of high resolution X-ray tomography: A review of the post-reconstruction analysis. *Spectrochim. Acta Part B At. Spectrosc.* **117**, 29–41 (2016).
28. C. Cao *et al.*, Emerging X-ray imaging technologies for energy materials. *Mater. Today* **34**, 132–147 (2020).
29. Z. Yang *et al.*, Probing dopant redistribution, phase propagation, and local chemical changes in the synthesis of layered oxide battery cathodes. *Adv. Energy Mater.* **11**, 2002719 (2021).
30. C. Wei *et al.*, Thermally driven mesoscale chemomechanical interplay in $Li_{0.5}Ni_{0.6}Mn_{0.2}Co_{0.2}O_2$ cathode materials. *J. Mater. Chem. A* **6**, 23055–23061 (2018).
31. M.-J. Zhang *et al.*, Cationic ordering coupled to reconstruction of basic building units during synthesis of high-Ni layered oxides. *J. Am. Chem. Soc.* **140**, 12484–12492 (2018).
32. C. Geng, A. Liu, J. R. Dahn, Impact of aluminum added to ni-based positive electrode materials by dry particle fusion. *Chem. Mater.* **32**, 6097–6104 (2020).
33. A. Le Bail, A. Jouanneaux, A qualitative account for anisotropic broadening in whole-powder-diffraction-pattern fitting by second-rank tensors. *J. Appl. Crystallogr.* **30**, 265–271 (1997).
34. K. Märker, P. J. Reeves, C. Xu, K. J. Griffith, C. P. Grey, Evolution of structure and lithium dynamics in $LiNi_{0.8}Mn_{0.1}Co_{0.1}O_2$ (NMC811) cathodes during electrochemical cycling. *Chem. Mater.* **31**, 2545–2554 (2019).
35. C. Xu, P. J. Reeves, Q. Jacquet, C. P. Grey, Phase behavior during electrochemical cycling of Ni-Rich cathode materials for Li-ion batteries. *Adv. Energy Mater.* **11**, 2003404 (2021).
36. R. Xu, L. S. de Vasconcelos, J. Shi, J. Li, K. Zhao, Disintegration of meatball electrodes for $LiNi_xMn_yCo_zO_2$ cathode materials. *Exp. Mech.* **58**, 549–559 (2018).
37. S. Li *et al.*, Mutual modulation between surface chemistry and bulk microstructure within secondary particles of nickel-rich layered oxides. *Nat. Commun.* **11**, 4433 (2020).
38. Y. Zhu, H. Pham, J. Park, A new aspect of the Li diffusion enhancement mechanism of ultrathin coating layer on electrode materials. *ACS Appl. Mater. Interfaces* **11**, 38719–38726 (2019).
39. J. Li *et al.*, Dynamics of particle network in composite battery cathodes. *Science* **376**, 517–521 (2022).
40. Y. Cao, T. D. Hatchard, R. A. Dunlap, M. N. Obrovac, Mechanofusion-derived Si-alloy/graphite composite electrode materials for Li-ion batteries. *J. Mater. Chem. A* **7**, 8335–8343 (2019).
41. Y. Liu *et al.*, TXM-Wizard: A program for advanced data collection and evaluation in full-field transmission X-ray microscopy. *J. Synchrotron Radiat.* **19**, 281–287 (2012).
42. X. Xiao, Z. Xu, F. Lin, W.-K. Lee, TXM-Sandbox: An open-source software for transmission X-ray microscopy data analysis. *J. Synchrotron Radiat.* **29**, 266–275 (2022).
43. X. Xiao, Z. Xu, D. Hou, Z. Yang, F. Lin, Rigid registration algorithm based on the minimization of the total variation of the difference map. *J. Synchrotron Radiat.* **29**, 1085–1094 (2022).
44. O. J. Borkiewicz *et al.*, The AMPIX electrochemical cell: A versatile apparatus for in situ X-ray scattering and spectroscopic measurements. *J. Appl. Crystallogr.* **45**, 1261–1269 (2012).
45. C. Prescher, V. B. Prakapenka, DIOPTAS: A program for reduction of two-dimensional X-ray diffraction data and data exploration. *High Press. Res.* **35**, 223–230 (2015).
46. B. H. Toby, R. B. Von Dreele, GSAS-II: The genesis of a modern open-source all purpose crystallography software package. *J. Appl. Crystallogr.* **46**, 544–549 (2013).

Downloaded from https://www.pnas.org by PURDUE UNIVERSITY LIBRARY on December 1, 2022 from IP address 128.210.126.199.